



Shear Deformation Behavior of Heterostructured Materials: Experimental and Numerical Analyses

Gang Hee Gu¹ · Shin-Yeong Lee² · Min Hong Seo³ · Jae-il Jang⁴ · Hyoung Seop Kim^{1,2,5,6,7}

Received: 11 October 2023 / Accepted: 6 November 2023
© The Author(s) under exclusive licence to The Korean Institute of Metals and Materials 2023

Abstract

In this study, the heterogeneous strengthening behavior in shear deformation was experimentally characterized and numerically modeled for the first time. Uniaxial tensile and simple shear tests were conducted to evaluate the mechanical behavior of Al/Steel/Al layered sheet and its monolithic layers. Contrary to expectations, the mechanical behavior of the layered sheet showed more outstanding performance compared to a simple calculation of the rule of mixtures in not only tensile deformation but also shear deformation, proving the heterogeneous strengthening effect in shear deformation as well. Moreover, the yield strength showed similar synergies in tensile and shear deformations, but the shear deformation exhibited a higher additional strengthening effect at the load before reaching fracture. This remarkable outcome is primarily attributed to the formation of a large amount of geometrically necessary dislocations near the heterogeneous interface in shear deformation than at tensile maximum load. Meanwhile, microstructure and deformation mechanism-based constitutive models were applied to finite element simulations of tensile and shear deformations. The numerically predicted stress–strain curves were compared to experimental results, indicating that microstructure-based constitutive models are reasonable for shear stress state as well as uniaxial tension state. Furthermore, dislocation density-based hardening model is better than conventional phenomenological isotropic hardening for extrapolation of large strain in simple shear test. This is mainly due to consideration of microstructural features in dislocation density-based hardening model.

Keywords Shear deformation · Heterostructured material · Layered sheet · Geometrically necessary dislocation · Finite element method

Abbreviations

FEM	Finite element method	RD	Rolling direction
TD	Transverse direction	GND	Geometrically necessary dislocation
BSE	Backscatter electron	DIC	Digital image correlation
EDS	Electron dispersive spectroscopy	SSD	Statistically stored dislocations
FE-SEM	Field emission scanning electron microscopy	IPF	Inverse pole figure
EBSD	Electron backscatter diffraction	E	Elastic modulus
		YS	Yield strength

✉ Shin-Yeong Lee
sylee413@postech.ac.kr

✉ Hyoung Seop Kim
hskim@postech.ac.kr

¹ Department of Materials Science and Engineering, Pohang University of Science and Technology (POSTECH), Pohang 37673, Republic of Korea

² Graduate Institute of Ferrous and Energy Materials Technology, Pohang University of Science and Technology (POSTECH), Pohang 37673, Republic of Korea

³ Technical Research Lab, POSCO, Incheon 21985, Republic of Korea

⁴ Division of Materials Science and Engineering, Hanyang University, Seoul 04763, Republic of Korea

⁵ Center for Heterogenic Metal Additive Manufacturing, Pohang University of Science and Technology (POSTECH), Pohang 37673, Republic of Korea

⁶ Institute for Convergence Research and Education in Advanced Technology, Yonsei University, Seoul 03722, Republic of Korea

⁷ Advanced Institute for Materials Research (WPI-AIMR), Tohoku University, Sendai 980-8577, Japan

UTS	Ultimate tensile strength
UEL	Uniform elongation
TEL	Total elongation
ROM	Rule of mixtures

1 Introduction

Metallic materials with excellent strength and ductility are always in high demand for their critical roles in structural applications. Structural metallic materials that satisfy both high strength and high ductility have various benefits, such as reducing component thickness and ensuring user safety in the construction industry, reducing greenhouse gas emissions, and facilitating complex forming in the automobile industry. However, an increase in either strength or elongation inevitably leads to a decrease in the other because strength and elongation are mutually exclusive factors in nature [1–3]. For example, Lee et al. [4] reported that there is a trade-off relationship between strength and elongation through various grain sizes depending on the annealing temperature of austenitic Fe–24Mn–4Cr–0.5C high-manganese steel. Malygin [5] also succeeded in improving the strength of polycrystalline aluminum by reducing the grain size, but the elongation was correspondingly reduced. As such, it is difficult to simultaneously enhance the tensile properties of strength and elongation with traditional strengthening mechanisms.

In recent decades, the heterostructure strategy through microstructural heterogeneities such as grain size, composition, phase, and texture has emerged as a representative method for improving tensile strength-ductility combinations [6–9]. This new strategy allows additional dislocations to accumulate between heterogeneous domains during tensile deformation, inducing an extra strengthening effect without loss of ductility [10–13]. There have also been several reports that it is possible to increase the ductility without being limited to the strength improvement effect depending on the combination of heterogeneous domains [14–16]. Fu et al. [17] fabricated heterostructured zirconium with simultaneously enhanced tensile strength and elongation compared to its coarse-grained counterpart by cold-rolling and subsequent annealing. Jin et al. [18] found that the elongation of clad materials was improved by the difference in the plastic instability behavior of constituent materials under tensile deformation and reported that the elongation of the clad sheet composed of aluminum alloy and stainless steel 439 exceeds that of the individual materials. Kim et al. [19] reported that the rule of mixtures calculated by the constituent monolithic layers is not consistent with the clad sheet due to the heterogeneous strengthening effect. Metallic materials manufactured from attempts to enhance strength and ductility through heterostructuring strategies were able

to successfully upgrade tensile properties more than homogeneous ones. However, studies on heterostructured metallic materials have limitations in that only the strengthening effect on tensile deformation mode has been discussed. Generally, metallic materials are subjected to various deformation modes such as compressive, shear, torsion, and bending as well as tension. This is because structural materials are manufactured to structures by metal forming processes, such as drawing, press, and extrusion, and the structures are exposed to various loading environments during service time. It is, therefore, necessary to demonstrate not only the deformation mechanism in tensile deformation but also the heterogeneous effect in other deformation modes [20–22].

Furthermore, various constitutive models have been employed to predict the deformation behavior of heterostructured metallic materials. Some studies used phenomenological constitutive models. Brown et al. [23] used the Johnson–Cook hardening model [24] to predict the temperature-dependent tensile behavior of heterostructured high entropy alloy. Wang et al. [25] also used the Johnson–Cook hardening model to predict the dynamic tensile behavior of heterostructured high entropy alloys. Moon et al. [26] used the phenomenological constitutive model to predict mechanical behavior in V-bending for stainless steel/carbon steel clad sheets. On the other hand, some studies used microstructural mechanism-based constitutive models. Zhao et al. [27] used the dislocation density-based hardening model to predict the tensile behavior of heterostructured laminates. Kim et al. [28] also used the dislocation density-based hardening model to predict the tensile behavior for the layered sheet composed of aluminum and steel. However, most previous studies have a limitation to applications of constitutive models to only uniaxial tensile tests. The constitutive models need to be validated for other deformation modes for the application of manufacturing and structural simulations.

In this study, the shear deformation mechanism at the heterogeneous interface of Al1050/low-carbon steel/Al1050 layered sheet was experimentally characterized and analyzed by numerical modeling with microstructural mechanism-based constitutive models. The layered sheet with Al1050 and low-carbon steel was selected because of their clear heterogeneous interfaces and large differences in strengths between the individual materials. This is the first report on the specific deformation mechanism of heterostructured materials under shear deformation mode. The shear-deformed microstructure and the finite element method (FEM) results validated the benefits of the heterogeneous interfaces in shear deformation in addition to tensile deformation. This study will contribute to the fundamental understanding as well as to the industrialization of heterostructured materials in terms of user safety as the first step in verifying the deformation mechanism of non-tensile deformation mode.

2 Experimental Procedures

2.1 Sample Preparation

To experimentally demonstrate heterogeneous interfaces under shear deformation, commercially available Al1050 alloy and low-carbon steel were used in this study. The reason why Al1050 and low-carbon steel were selected is that their strength heterogeneity is high and intermetallic compounds are not formed at the interface below 540 °C [15]. The layered sheet was prepared by sequentially stacking Al1050, low-carbon steel, and Al1050 plates and bonding them through a roll-to-roll process. After the roll-to-roll process, the thickness of the Al1050, low-carbon steel, and Al1050 layers was measured to be 0.2 mm, 0.6 mm, and 0.2 mm, respectively. The as-rolled layered plate was subjected to annealing heat treatment at 500 °C for 1 h. The individual plates were also produced through the same thermomechanical processes for quantitative comparisons. All metal plates used in the experiments were provided by POSCO.

2.2 Microstructural Characterization

Before microstructural analyses, the transverse direction (TD) planes of all the samples were mechanically polished using 600, 800, and 1200 grit papers; then, they were finely polished for 10 min each with 3 μm , 1 μm , 0.25 μm diamond suspensions, and slightly etched for 20 min with colloidal silica suspension. Backscatter electron (BSE) and electron dispersive spectroscopy (EDS) analyses were performed using field emission scanning electron microscopy (FE-SEM; JSM-7800F PRIME, JEOL Ltd., Japan) to investigate the fraction of each layer and the absence of intermetallic compounds.

The effect of heterogeneity in shear deformation was demonstrated by comparatively analyzing the tensile-deformed and shear-deformed microstructures using the electron backscatter diffraction (EBSD) technique. The EBSD experiments were conducted on an FE-SEM (FE-30XL, Philips, The Netherlands) equipped with an EBSD detector. The step size of EBSD was set to 25 nm to represent the geometrically necessary dislocation (GND) maps more accurately. The collected EBSD data were interpreted with orientation imaging microscopy software (TSL OIM Analysis 7).

2.3 Mechanical Properties Evaluation

Uniaxial tensile tests and Vickers microhardness tests were used to evaluate the mechanical properties of Al1050 and low-carbon steel constituting the layered sheet. Before

performing the tensile test, the rolling direction (RD) of the dog bone-shaped tensile specimens with a gauge length of 6.4 mm and a gauge width of 2.5 mm was cut using wire-cut electrical discharge machining from each metal plate. No polishing was conducted prior to tensile testing to maintain the fraction of constituent layers in the layered sheet. Tensile tests were performed with a universal testing machine (Instron 1361, Instron Corp., USA) at a strain rate of 10^{-3} s^{-1} and at room temperature conditions. The digital image correlation (DIC) equipment (ARAMIS 12M, GOM Optical Tech., Germany) and ARAMIS Professional 2021 software were used to precisely estimate the length change during tension. The hardness of Al1050 and low-carbon steel was assessed by performing a Vickers microhardness test using a Vickers microhardness tester (Future-Tech FM-700, Japan).

For the simple shear test, a rectangular specimen with RD of 50 mm and TD of 16 mm was machined from Al1050, low-carbon steel, and layered sheet. The simple shear tests were performed by a 500 kN MTS universal tension–compression machine with anti-buckling equipment. The average shear strain of the specimens was obtained using a DIC camera (GRAS-50S5M-C, FLIR Systems Inc., USA) and VIC-2D software. The simple shear test was performed by fixing one side of the rectangular specimen and moving the other grip down, as illustrated in Fig. 1. A detailed description of the simple shear tester is provided in a previous study [29].

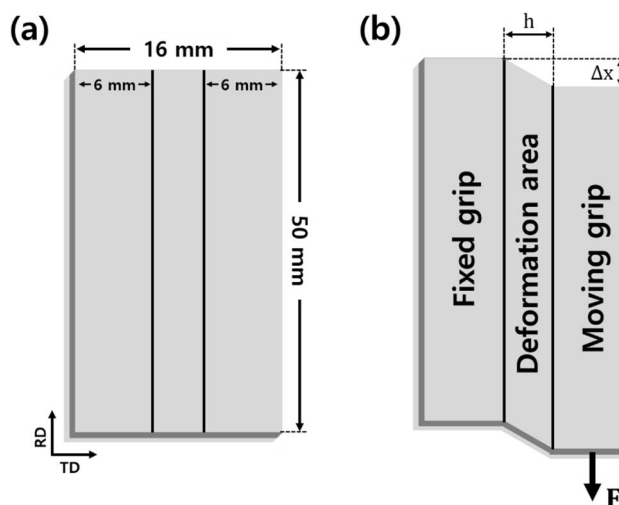


Fig. 1 Schematic illustration of **a** before and **b** after deformation in the simple shear test

3 Numerical Modeling Procedures

3.1 Constitutive Models

The microstructure and deformation mechanism-based constitutive models were employed to analyze mechanical behaviors numerically. For elasticity, the conventional isotropic Hooke's law was used. Also, the conventional macroscopic elasto-plasticity theory judges the plastic state when the yield condition is zero. The yield condition is defined as follows:

$$\Phi(\boldsymbol{\sigma}) = \bar{\sigma}(\boldsymbol{\sigma}) - \sigma_r(\bar{\epsilon}), \quad (1)$$

where Φ is the yield condition, $\boldsymbol{\sigma}$ is the Cauchy stress tensor, $\bar{\sigma}$ is the equivalent stress, σ_r is the reference isotropic hardening, and $\bar{\epsilon}$ is the equivalent strain. The von-Mises isotropic yield function was employed to consider multi-axial mechanical behavior. The equivalent stress of this yield function is defined as follows:

$$\bar{\sigma}(\boldsymbol{\sigma}) = \frac{1}{\sqrt{2}} \left[(\sigma_{11} - \sigma_{22})^2 + (\sigma_{22} - \sigma_{33})^2 + (\sigma_{33} - \sigma_{11})^2 + 6(\sigma_{12}^2 + \sigma_{23}^2 + \sigma_{13}^2) \right]^{1/2}, \quad (2)$$

For the reference isotropic hardening, the dislocation density-based isotropic hardening for heterostructured materials [12] was employed. For the dislocation model, the reference isotropic hardening is defined based on Taylor hardening law [30]. The equation is:

$$\sigma_r(\bar{\epsilon}) = \tau_0 + \alpha M G b (\sqrt{\rho_{SSD}} + \sqrt{\rho_{GND}}), \quad (3)$$

where τ_0 is the lattice friction stress, α is a dislocation interaction parameter, M is the Taylor factor, G is the shear modulus, and b is the magnitude of the Burgers vector. ρ_{SSD} and ρ_{GND} mean densities of statistically stored dislocations (SSD) and GND, respectively. Both dislocation densities are evolved by the increase of equivalent strain. The evolution of ρ_{SSD} is selected by the Kocks-Mecking-Estrin equation [31] and it is defined as follows,

$$\frac{d\rho_{SSD}}{d\bar{\epsilon}} = M \left(\frac{1}{bD} \right) + \frac{k}{b} \sqrt{\rho_{SSD}} - f \rho_{SSD}, \quad (4)$$

where D means the average grain size, k is a dislocation accumulation parameter, and f is a dislocation annihilation parameter. The evolution of ρ_{GND} selected in Reference [28] is as follows:

$$\frac{d\rho_{GND}}{d\bar{\epsilon}} = \frac{M\theta}{bD} D_{loc}, \quad (5)$$

where θ and D_{loc} mean the local deformation parameter and the geometrical position, respectively. The local deformation

parameter (θ) evolves with respect to the equivalent strain as follows:

$$\theta = \theta_0 \exp(-\lambda \bar{\epsilon}) \quad (6)$$

where θ_0 and λ are the initial deformation parameter and coefficient, respectively. This evolution equation expresses the characteristic of GND, indicating that the rate of GND storage tends to saturate as plastic deformation increases. In other words, the generation of GND is decelerated by plastic deformation because many existing dislocations prevent the generation of new dislocations through repulsion between dislocations. The geometrical position (D_{loc}) means the distance between the geometrical dislocation and interface of the layered sheet. The FEM implementation of the geometrical position (D_{loc}) will be dealt in the next section.

3.2 Finite Element Modeling

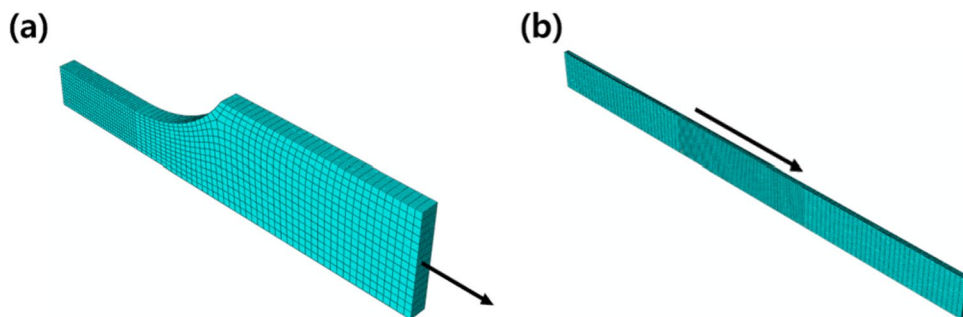
The uniaxial tensile and simple shear tests in Sect. 2.3 were numerically modeled by commercial finite element software, ABAQUS. The implicit FEM and the 3D brick solid element (C3D8R) were used. The previous constitutive models were implemented into the user material subroutine, UMAT using FORTRAN language. The recently developed non-iterative stress projection method, originally referenced in the paper [32], was implemented. This approach was used for all simulations to reduce the huge simulation time for solid elements. The non-iterative stress projection method offers a better combination of speed and accuracy in stress calculation compared to the other conventional iterative stress integration methods because it does not require iteration processes. The geometrical position (D_{loc}) was implemented using the following equation:

$$D_{loc} = \delta \frac{z-z_0}{z_0} \quad (7)$$

where δ is a steepness parameter, z is the z -coordinate of the integration point, and z_0 is the z -coordinate of the interface between Al1050 and low-carbon steel. It means that the z -coordinate of integration point was normalized based on the z -coordinate of the interface. This adjustment is made to consider the phenomenon that the closer to the interface, the more GND is generated.

One-eighth and a half of the specimens were modeled for the uniaxial tensile and simple shear tests, respectively. Stress-strain curves can be extracted from simulations in the same way that they are measured in experiments. Based on the stress-strain curves, a sensitivity study was performed to decide mesh size and the number of through-thickness elements. For the uniaxial tensile test, 0.1 mm² mesh size in the central region and 10 through-thickness elements were selected. On the other hand, for the simple shear test, 0.2

Fig. 2 Finite element models for **a** the uniaxial tensile and **b** the simple shear tests



mm^2 mesh size in the central region and 10 through-thickness elements were selected. Figure 2 shows the finite element models for the uniaxial tensile and simple shear tests.

4 Results

4.1 Initial Microstructure

Figure 3a shows the BSE image for the entire area of the Al1050/low-carbon steel/Al1050 layered sheet. The layered plate is clearly divided into a relatively dark Al1050 layer and a bright low-carbon steel layer. The fractions of Al1050 and low-carbon steel regions calculated using an image analysis software (ImageJ Ver. 1.50i, National Institutes of Health, USA) were 40.33% and 59.67%, respectively, consistent with the measured thicknesses of 0.2 mm/0.6 mm/0.2 mm. Along with the EDS elemental distribution maps in Fig. 3b, c, it was confirmed that no intermetallic compound was generated at the interfacial region during the annealing heat treatment at 500 °C for 1

h. The EDS line profile result indicates that the interface between Al1050 and low-carbon steel is bonded by a short interdiffusion of $\sim 0.8 \mu\text{m}$ (Fig. 3d).

Figure 4 shows EBSD inverse pole figure (IPF) maps and GND maps of the Al1050, low-carbon steel, and interfacial region of the layered sheet. From the low-magnification EBSD results, the average grain size of Al1050 was measured to be $34.10 \pm 12.83 \mu\text{m}$, and low-carbon steel was measured as $15.35 \pm 6.15 \mu\text{m}$. The difference in grain size between Al1050 and low-carbon steel is due to various factors such as grain size before bonding, degree of deformation during processing, and difference in their grain growth driving force. The initial GND densities of Al1050 and low-carbon steel calculated from Fig. 4d, e are $1.27 \times 10^{14} \text{m}^{-2}$ and $7.99 \times 10^{13} \text{m}^{-2}$, respectively. Although Al1050 has a lower microstructural evolution (i.e., recovery, recrystallization, and grain growth) temperature than low-carbon steel, the dislocation density was measured to be higher. It can be inferred that the relatively soft Al1050 plate underwent more deformation during the roll-to-roll process. The phase boundaries

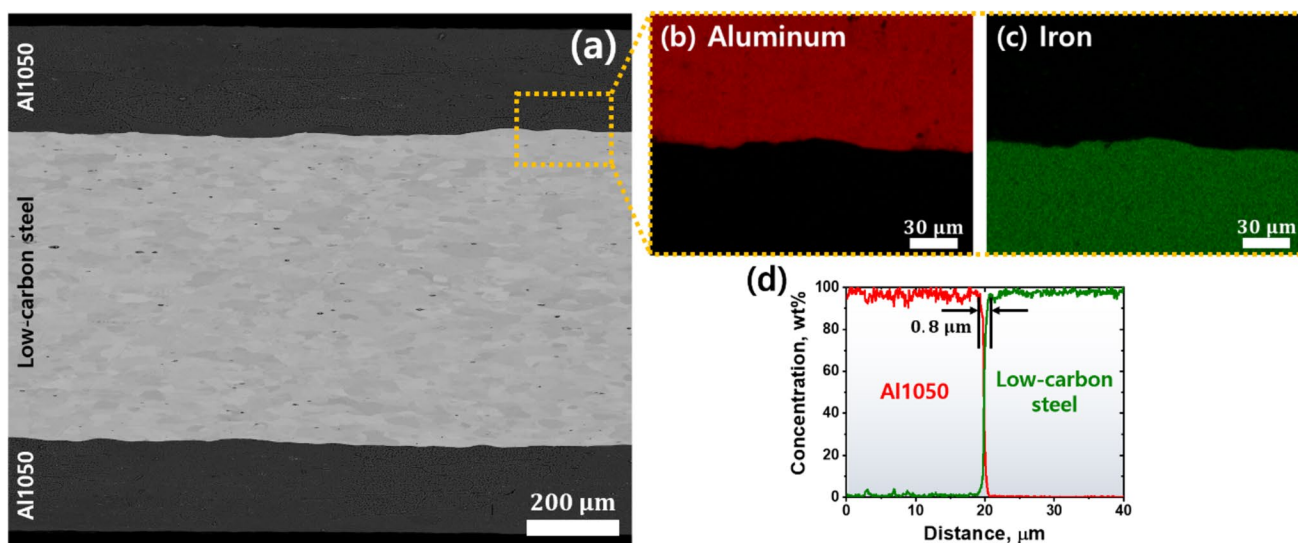


Fig. 3 **a** BSE image of Al1050/low-carbon steel/Al1050 layered sheet. **b**, **c** Magnified EDS elemental distribution maps and **d** EDS line profile in the interfacial region. In the EDS maps and line profile, red and olive colors indicate aluminum and iron elements, respectively

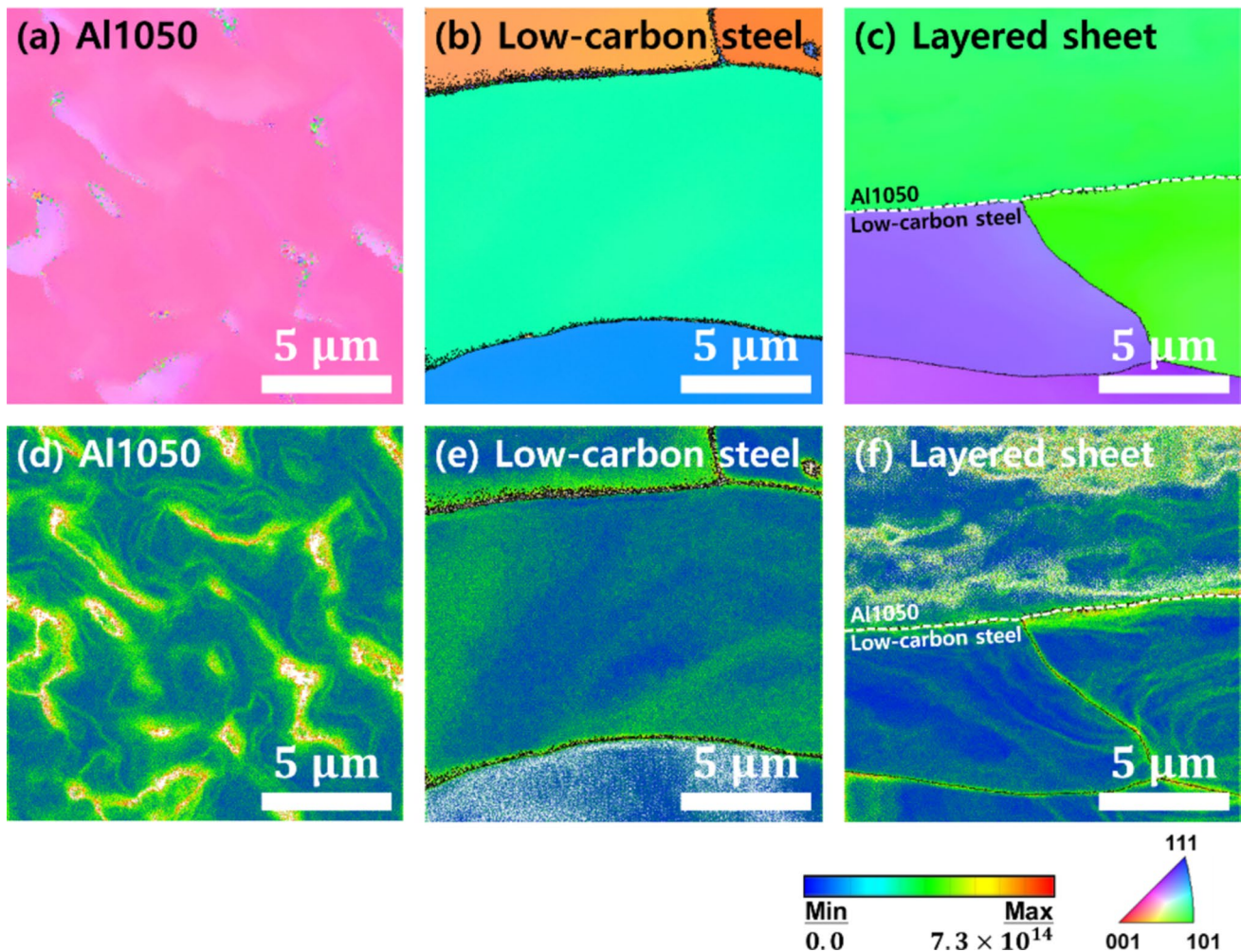


Fig. 4 a, b, c EBSD IPF maps and d, e, f GND maps of a, d Al1050, b, e low-carbon steel, and c, f interfacial region of the layered sheet

and grain boundaries showed higher GND densities than the grain inside because they are a kind of defect-like dislocations.

4.2 Tensile Properties and Vickers Microhardness

Figure 5a represents the tensile properties of Al1050, low-carbon steel, and layered sheet. Table 1 summarizes the tensile properties: Elastic modulus (E), yield strength (YS),

ultimate tensile strength (UTS), uniform elongation (UEL), and total elongation (TEL). Elastic modulus was calculated using the method proposed in Ref. [33]. The rule of mixtures (ROM) in Table 1 was calculated from tensile testing results of Al1050 and low-carbon steel and BSE micrograph (Figs. 3a and 5a). Interestingly, the tensile properties of the layered sheet outperformed ROM in all respects except the elastic modulus. The YS and UTS were further strengthened by ~ 22.97 MPa and ~ 24.14 MPa, respectively. The UEL

Fig. 5 a Tensile testing results of Al1050, low-carbon steel, and layered sheet. b Vickers microhardness results of Al1050 and low-carbon steel

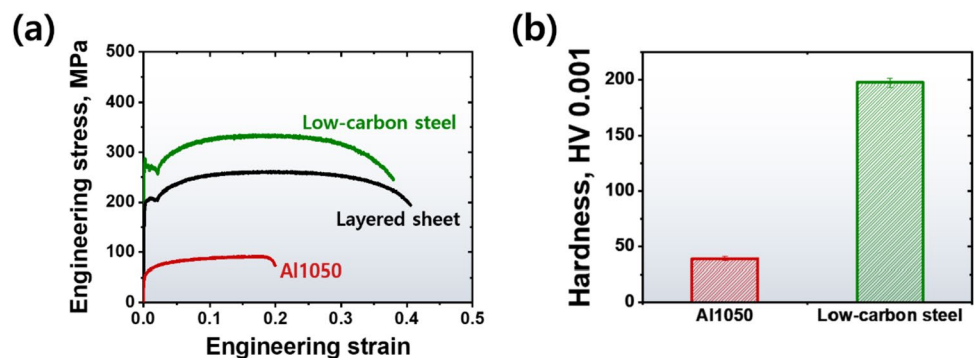


Table 1 Summary of tensile properties of Al1050, low-carbon steel, ROM, and layered sheet

	E, GPa	YS, MPa	UTS, MPa	UEL, %	TEL, %
Al1050	44.96	54.91 ± 2.9	91.34 ± 3.2	17.21 ± 2.5	19.96 ± 2.1
Low-carbon steel	171.17	264.25 ± 2.2	334.90 ± 3.0	17.01 ± 1.6	37.90 ± 2.5
ROM	120.68	180.51	237.48	17.09	30.72
Layered sheet	120.88	203.48 ± 3.5	261.62 ± 1.2	19.62 ± 1.5	40.59 ± 1.5

Tensile tests were repeated three times for reliability

and TEL increased by ~2.53% and ~9.87%, respectively, and even the layered sheet had a higher elongation than the individual Al1050 and low-carbon steel. Not only the layered sheet but also the individual Al1050 and low-carbon steel were in good agreement with the tensile stress–strain curves obtained by removing the counterpart material by chemical etching in our previous research [19]. This observation indicates that the Al1050 and low-carbon steel used in this study well simulate the constituent materials in the layered sheet. Furthermore, such synergy of strength and elongation by heterostructuring has often been reported in heterostructured materials [14–19]. The extra strengthening mainly occurs because additional dislocations are generated by the strength heterogeneity at the heterogeneous interfaces [16], and the advantage in ductility is primarily attributed to differences in plastic instability [17].

The Vickers microhardness results for Al1050 and low-carbon steel are shown in Fig. 5b. The Vickers microhardness values of Al1050 and low-carbon steel were measured as 39.06 ± 1.65 kg/mm² and 197.38 ± 3.74 kg/mm², respectively. The tensile testing and Vickers microhardness testing results demonstrate that Al1050 and low-carbon steel have strength heterogeneity, with Al1050 acting as a soft domain, and low-carbon steel acting as a hard domain.

4.3 Shear Properties

Shear stress–shear strain curves in shear deformation for Al1050, low-carbon steel, and the layered sheet are displayed in Fig. 6, and Table 2 summarizes indicators representing shear properties: 0.2% offset strength and maximum strength. Unlike the tensile testing results (Fig. 5a and Table 1), the shear deformation does not reveal plastic instability called necking, so UEL and TEL are not defined. The shear stress was obtained by dividing the force measured in the load cell by the cross-sectional area along the whole specimen length as for tensile stress calculation. The simple shear test was finished when the load value started to decrease due to fracture or buckling near the tips of the specimen, and the maximum shear strength was defined as the maximum value before the load decreased. Meanwhile, the shear strain was not measured uniformly over the entire specimen during the deformation, especially near the tips of the shear specimen.

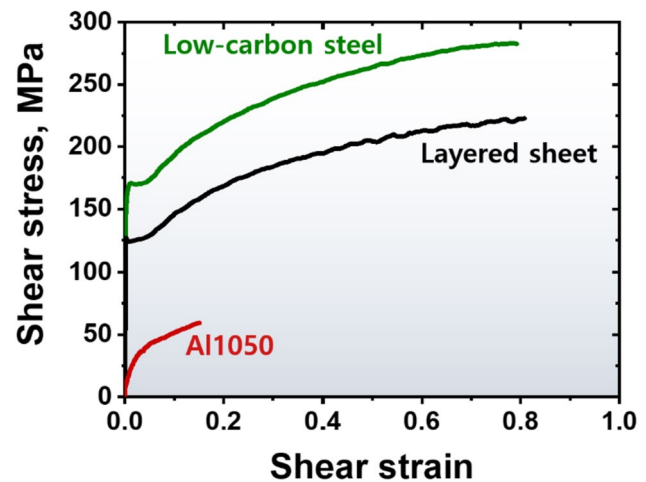


Fig. 6 Shear stress versus shear strain curves of Al1050, low-carbon steel, and layered sheet

Table 2 Shear 0.2% offset strength and maximum strength for Al1050, low-carbon steel, ROM, and layered sheet

	0.2% offset strength, MPa	Maximum strength, MPa
Al1050	35.10 ± 0.36	59.37 ± 0.72
Low-carbon steel	169.86 ± 1.35	282.98 ± 1.31
ROM	115.96	193.54
Layered sheet	126.74 ± 1.52	222.78 ± 1.28

The shear tests were repeated three times

Therefore, the value of the shear strain was determined as the average of the region having homogeneous strain distribution using the DIC technique. The validity of the shear strain obtained in this way was assessed by comparison with FEM simulations in a previous study [29].

The shear properties of Al1050 and low-carbon steel were consistent with tendencies of tensile and Vickers microhardness results in Fig. 5. Al1050, a region with low tensile strength and Vickers microhardness value, exhibited the lowest 0.2% offset strength and maximum strength of 35.10 ± 0.36 MPa and 59.37 ± 0.72 MPa, respectively. Reaching maximum strength at low shear strain also corresponded to having low ductility in tensile deformation.

Low-carbon steel with high tensile strength and Vickers microhardness value showed the highest shear strength with 0.2% offset strength of 169.86 ± 1.35 MPa and maximum strength of 282.98 ± 1.31 MPa.

The 0.2% offset strength of the layered sheet was 126.74 ± 1.52 MPa and the maximum strength was 222.78 ± 1.28 MPa, showing values between the A11050 and low-carbon steel. The layered sheet achieved shear strengths exceeding the calculated ROM from the A11050 and low-carbon steel, but the values of strength increase by heterogeneity were quite different compared to the tensile deformation. In the tensile test, the strengthening effect by heterostructuring showed similar values of ~ 22.97 MPa and ~ 24.14 MPa for YS and UTS, respectively (Fig. 5a). On the other hand, the 0.2% offset strength and maximum strength of layered sheet increased by ~ 10.78 MPa and ~ 29.24 MPa, respectively, compared to those of ROM, indicating a greater strengthening effect in the later stage than in the early stage of shear deformation. It will be dealt with in detail in Sect. 5.1.

4.4 Parameter Identification

The parameter identification for constitutive models in Sect. 3.1 was conducted with the tensile testing results in Sect. 4.2. The inverse identification method was used for parameter identification. The details of the inverse identification procedure [34] are as follows. The finite element simulation of tensile deformation in Sect. 3.2 was conducted with initial coefficients. Then, a difference in true stress–strain curves between the experiment and simulation was calculated by the least square method. To minimize the difference between experiments and simulations, many trials were repeated following the Nelder-Mead simplex optimization algorithm.

The parameters for single materials, A11050 and low-carbon steel, were identified first with the tensile test results. The shear modulus was calculated using the elastic modulus in Table 1 and Poisson's ratio, which is usually assumed to be 0.33 for metals. The Taylor factor (M) and the magnitude of Burger's vector (b) were assumed to be 3.06 and 2.54×10^{-7} mm, respectively. The grain size (D) was selected from EBSD results in Sect. 4.1. Therefore, only four parameters (τ_0 , α , k , and f) were identified using the inverse identification method. Then, the tensile stress–strain curve of the layered sheet was used to identify GND-related parameters (θ_0 and λ). The steepness parameter (δ) was assumed to be 10^4 . In the tensile test simulation of the layered sheet, it was assumed that the GND effect was generated only for A11050 based on observations from a previous study [28]. Table 3 summarizes all identified parameters for A11050 and low-carbon steel.

Table 3 Identified parameters of the constitutive models for A11050 and low-carbon steel

	A11050	Low-carbon steel
τ_0 [MPa] [†]	34.51	247.19
α [†]	0.7730	0.0955
M	3.06	3.06
G [MPa]	16.9	64.35
b [mm]	2.54×10^{-7}	2.54×10^{-7}
D [mm]	0.0341	0.0153
k [†]	0.0009	0.0392
f [†]	2.74	2.99
θ_0 [†]	50.77	1
λ [†]	0.0033	0
δ	10^4	0

[†]Inversely identified parameters

4.5 Numerical Prediction

The true stress–strain curves of A11050, low-carbon steel, and layered sheets in tensile deformation were predicted by simulation with the dislocation density-based isotropic hardening model, as shown in Fig. 7a. For A11050 and low-carbon steel, the predictions of the simulation follow the experimental results well. This means that inverse identification was completed successfully. For the layered sheet, the simulation without considering GND terms, which is the same for ROM, shows a clear underestimation of flow stress. On the other hand, the simulation considering GND terms predicted flow stress well without underestimation. This is mainly due to the heterogeneous strengthening effect.

Furthermore, constitutive models were applied to simple shear tests. For simulation of multi-axial deformation, the von-Mises isotropic yield function in Sect. 3.1 was used. The numerical prediction of stress–strain curves of A11050, low-carbon steel, and layered sheets in simple shear tests is shown in Fig. 7b. Although some underestimation was observed for A11050 and low-carbon steel, the prediction for shear strength in the von-Mises yield function is acceptable for both materials. In addition, prediction considering GND effect shows better than prediction without GND effect. This is consistent with results of tensile test simulation. It indicates that the dislocation model considering GND effect is effective in shear stress state even though its parameters are identified only in tensile deformation. Although a slight underestimation was found for the Al and low-carbon steel single sheets, the dislocation model predicted the layered sheet very well. This suggests that the formation of GND is the main determinant of hardening in layered sheets. Moreover, predictability of dislocation model for layered sheet until large strain is verified. Although the maximum strain of tensile test was smaller than that of simple shear test, the

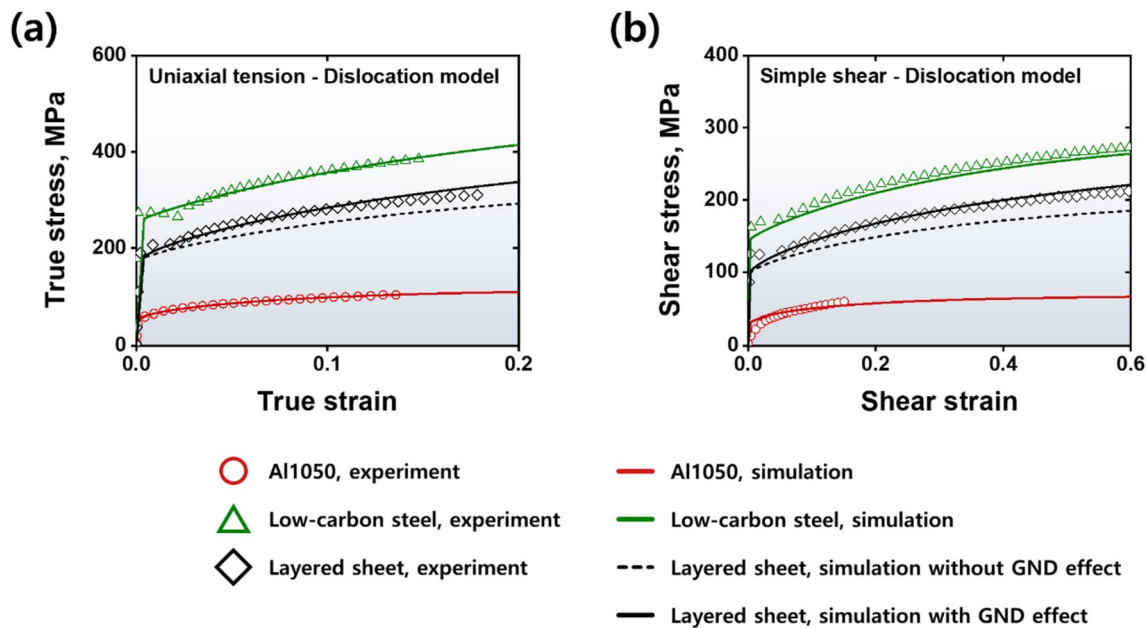


Fig. 7 a Numerical prediction of true stress vs. true strain curves of the Al1050, low-carbon steel, and layered sheets in the tensile test using the dislocation density-based isotropic hardening model;

b Numerical prediction of shear stress vs. shear strain curves of the Al1050, low-carbon steel, and layered sheets in the simple shear test using the dislocation density based isotropic hardening model

prediction of dislocation model follows the whole trend well in simple shear test. This observation will be discussed more in the next section.

5 Discussion

5.1 Heterogeneous Strengthening Effect in Shear Deformation

A comparison of the layered sheet with monolithic Al1050 and low-carbon steel demonstrated that shear deformation can achieve a heterogeneous strengthening effect as in tensile deformation (Fig. 6 and Table 2). The synergistic strengthening of YS in tensile deformation is ~ 22.97 MPa and the corresponding 0.2% offset strength in shear deformation is ~ 10.78 MPa. The von-Mises yield criterion defines a 0.2% offset strength in the shear test to be 0.577 times YS in the tensile test [35]. In terms of the yield onset relationship, the additional strengthening effect of shear deformation using the von-Mises yield criterion was converted to ~ 18.68 MPa in tensile deformation. Considering that the YS of the layered sheet exceeded the ROM by ~ 22.97 MPa in tension, both tensile and shear deformations can benefit from a similar degree of heterogeneous strengthening effect at the beginning of plastic deformation.

The tensile UTS and the maximum shear strength, which are the highest stresses in each deformation mode, exhibited different results from the yield onset. There is no

well-established theory for maximum shear strength, such as the yield criterion at the beginning of plastic deformation. However, it is generally considered for product design purposes that maximum shear strength is equal to 60% of tensile UTS [36]. Nevertheless, the investigated layered sheet showed additional strength enhancements of ~ 24.14 MPa and ~ 29.24 MPa in tensile UTS and maximum shear strength, respectively, compared to the ROM of the individual materials. Considering that the maximum shear strength is 60% of the tensile UTS, the additional strengthening effect at maximum shear strength was converted to ~ 48.73 MPa in the tensile UTS. These results obviously indicate that the shear and tensile deformations have similar heterogeneous strength improvement in the early stage of plastic deformation but show more effective strength enhancement in the shear deformation in the later stage of deformation.

Figure 8a, b are the IPF and GND maps at 15% and 80% applied shear strain, respectively. It clearly demonstrates that GNDs thickly accumulate at the heterogeneous domain interfaces even under shear deformation, similar to the result of tensile deformation [15]. Figure 8c, d show the GND density profiles near the Al1050/low-carbon steel interface under tensile and shear deformations, respectively. Both tensile deformation and shear deformation accumulated GNDs at the heterogeneous interface as plastic deformation progressed but with slight differences. In the case of tensile deformation, both at the beginning of plastic deformation and UTS exhibited accumulated GNDs by approximately $1.69 \mu\text{m}$ near the heterogeneous interface. It can be

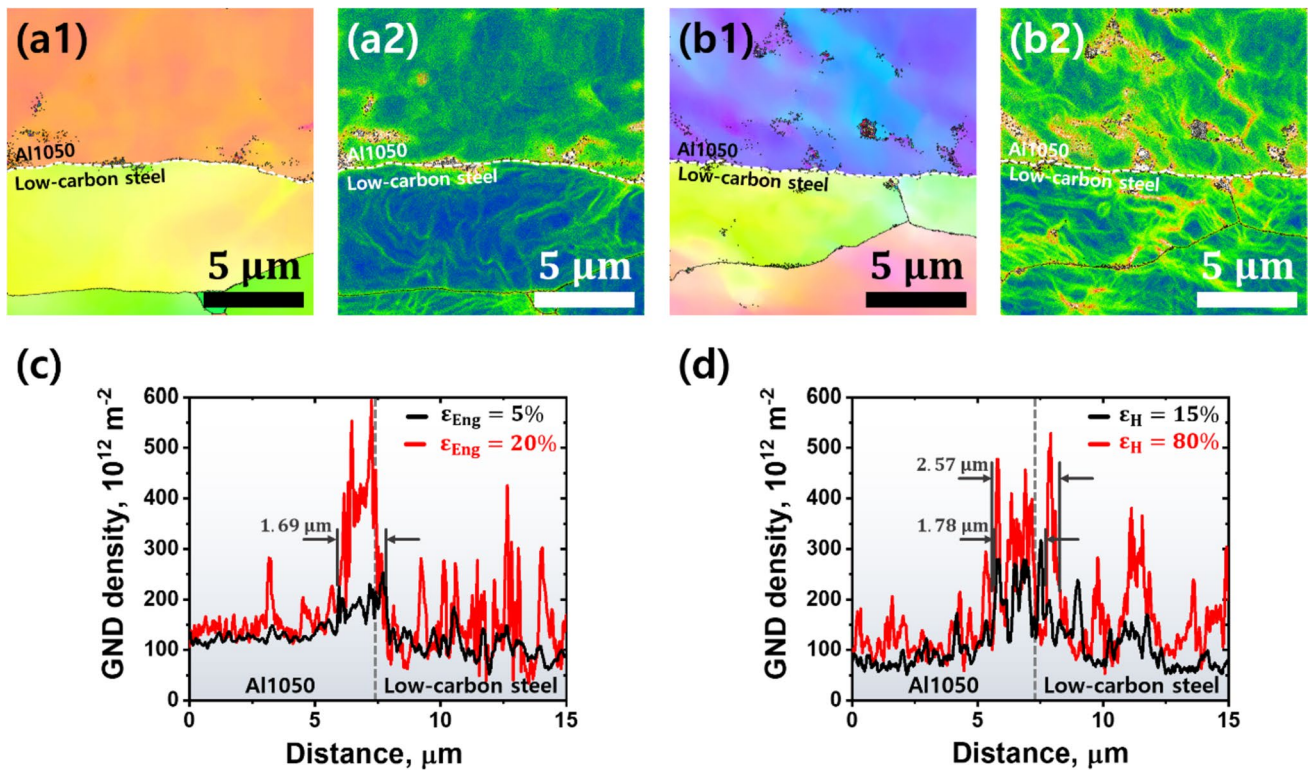


Fig. 8 EBSD IPF maps and GND maps at **a** 15% and **b** 80% applied shear strain. GND density profiles near the Al1050/low-carbon steel interface at **c** 5% and 20% applied tensile strain and **d** 15% and 80% applied tensile strain

demonstrated that there was a limit to the GND accumulation even at maximum load, which results in a similar level of heterogeneous strengthening effect in tensile UTS and YS. On the other hand, in the shear-deformed heterogeneous interface, GND was additionally accumulated by a distance of about 0.79 μm at the maximum shear strength with large deformation compared to the initial stage of plastic deformation. These GND line profile results verify the difference in the heterogeneous strengthening behavior of tensile deformation and shear deformation at the yield onset and maximum load.

5.2 Deformation Characterization in a Simple Shear Test

To discuss the strain ranges in tensile and shear deformation modes, the von-Mises equivalent strain formula defined by Eq. (8) was used [36]:

$$\bar{\epsilon}_{vm} = \frac{2}{3} \sqrt{\frac{3}{2}(\epsilon_{11}^2 + \epsilon_{22}^2 + \epsilon_{33}^2) + \frac{3}{4}(\gamma_{12}^2 + \gamma_{23}^2 + \gamma_{31}^2)}, \quad (8)$$

where ϵ_{11} , ϵ_{22} , ϵ_{33} , γ_{12} , γ_{23} , and γ_{31} indicate components of the strain tensor. The shear strain at the maximum shear strength of the layered sheet was 80.98%, which corresponds

to the von-Mises equivalent strain of $\sim 66.13\%$ according to Eq. (8). This converted von-Mises equivalent strain value is about three times higher than 19.62%, which is the strain corresponding to the UTS of the layered sheet in the tensile test. The difference between applied strain in tensile deformation and shear deformation at maximum load was primarily due to their deformation behavior. In tensile deformation, the material elongates only in the axial direction, and plastic instability occurs in which stress and strain are concentrated locally after UTS [37, 38] (Fig. 9a). This is referred to as the neck phenomenon, and strain hardening behavior does not appear and the load decreases in the post-necking elongation regime after UTS. That is, due to the concentration of local stress and strain by plastic instability in the post-necking elongation regime, the tensile UTS does not show deformation behavior at large deformation despite the maximum load. In shear deformation, strain is applied to the specimen uniformly up to the maximum shear strength without plastic instability, and fracture occurs at that strain (Fig. 9b). Figure 9a1, b show von-Mises equivalent strain distributions at tensile UTS and maximum shear strength, respectively, and it was confirmed that the load maximum in the shear test exhibited a higher strain distribution. Also, the occurrence of plastic instability after UTS was visually validated in Fig. 9a2. Maximum shear strength can accommodate more

Fig. 9 Von-Mises equivalent strain distribution maps at **a1** tensile UTS, **a2** after tensile neck onset, and **b** maximum shear strength

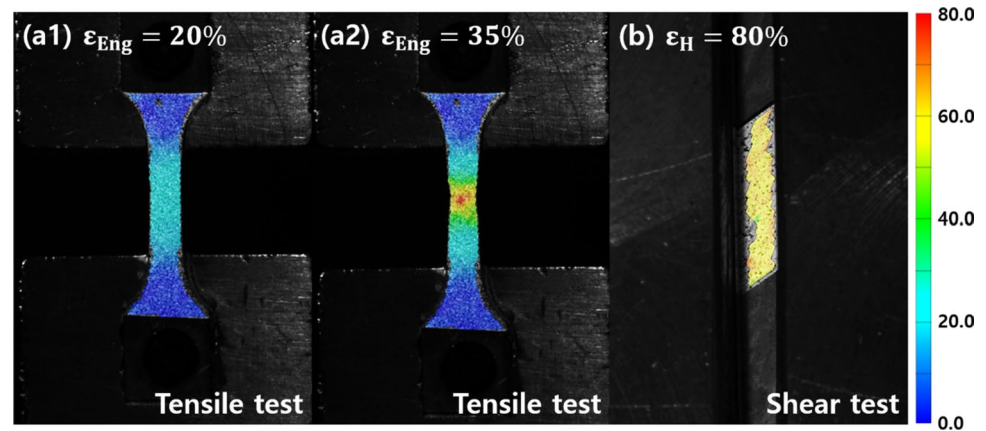


Table 4 Identified parameters of the Swift-modified Voce model for Al1050 and low-carbon steel

Swift-modified Voce	K	ϵ_0	n	σ_y	ρ	σ_b	η
Al1050	130.08	1.62×10^{-3}	0.1638	3.9012	35.45	1.055	10.31
Low-carbon steel	131.68	0.215	1.97×10^{-7}	120.55	1	173.75	10

deformation than the tensile UTS, which causes more dislocation formation and accumulation. Because dislocations accumulated at the dissimilar domain interfaces are the main cause of heterogeneous strengthening, the greater synergistic strengthening at maximum shear strength than tensile UTS can be explained by the difference in applied strain.

We concluded that (1) the heterogeneous strengthening behavior in shear and tensile deformations is similar and (2) the predominant additional strengthening effect in the maximum shear strength compared to the tensile UTS is simply the difference in applied strain. To support this outcome, the strengths of layered sheet and ROM were compared in terms of percentage. In tensile yield strength and shear 0.2% offset strength, the layered sheet showed additional strengthening of $\sim 12.73\%$ and $\sim 9.30\%$ over ROM, respectively. Meanwhile, the layered sheet exhibited $\sim 10.17\%$ and $\sim 15.11\%$ higher strength than ROM in tensile UTS and maximum shear strength, respectively. Although there are some deviations, by and large, the degree of heterogeneous strengthening effect in tensile and shear deformations is identical. The reasonable prediction of the dislocation density-based isotropic hardening model considering GND effect for both tensile and shear deformation modes (Fig. 7) also supports the similarity. Therefore, these results obviously indicate that the heterogeneous strengthening behavior in shear and tensile deformations are similar.

The dislocation density-based isotropic hardening model shows reasonable prediction until a relatively large strain in the simple shear test, even if the parameters are identified only in the tensile test, which shows a relatively small strain. The reasonable extrapolation of reference isotropic hardening is

important because some structural applications, i.e., crush and forming simulations, require large strain regions.

To compare the predictability of the dislocation model, one of the phenomenological isotropic hardening models, the Swift-modified Voce model, is selected. The equation is:

$$\sigma_r(\bar{\epsilon}) = K(\epsilon_0 + \bar{\epsilon})^n + \sigma_y + \rho\bar{\epsilon} + \sigma_b(1 - \exp(-\eta\bar{\epsilon})), \quad (9)$$

where K , ϵ_0 , n , σ_y , ρ , σ_b , and η are the fitting parameters. This equation is usually used for sheet metal forming simulation in references [34, 39]. The inverse identification explained in Sect. 4.4 is applied to the Swift-modified Voce model. The identified parameters for Al1050 and low-carbon steel are listed in Table 4.

Then, the Swift-modified Voce model was used for the tensile and simple shear simulations. Figure 10 shows the numerical predictions for the tensile and simple shear tests with the Swift-modified Voce models. The stress–strain curve prediction for low-carbon steel in the tensile test is reasonable because the parameters are identified in the tensile test. However, the stress–strain curve prediction for low-carbon steel in the simple shear test tends to be underestimated. This indicates that the extrapolation of the Swift-modified Voce model is not appropriate, even if the number of fitted parameters for the Swift-modified Voce model is larger than those for the dislocation density-based hardening model. The number of fitted parameters for the dislocation density-based hardening model is only four because other parameters can be decided using microstructure information. Therefore, this comparison suggests that considering microstructure characteristics can be helpful to predict hardening behavior until large strain regions.

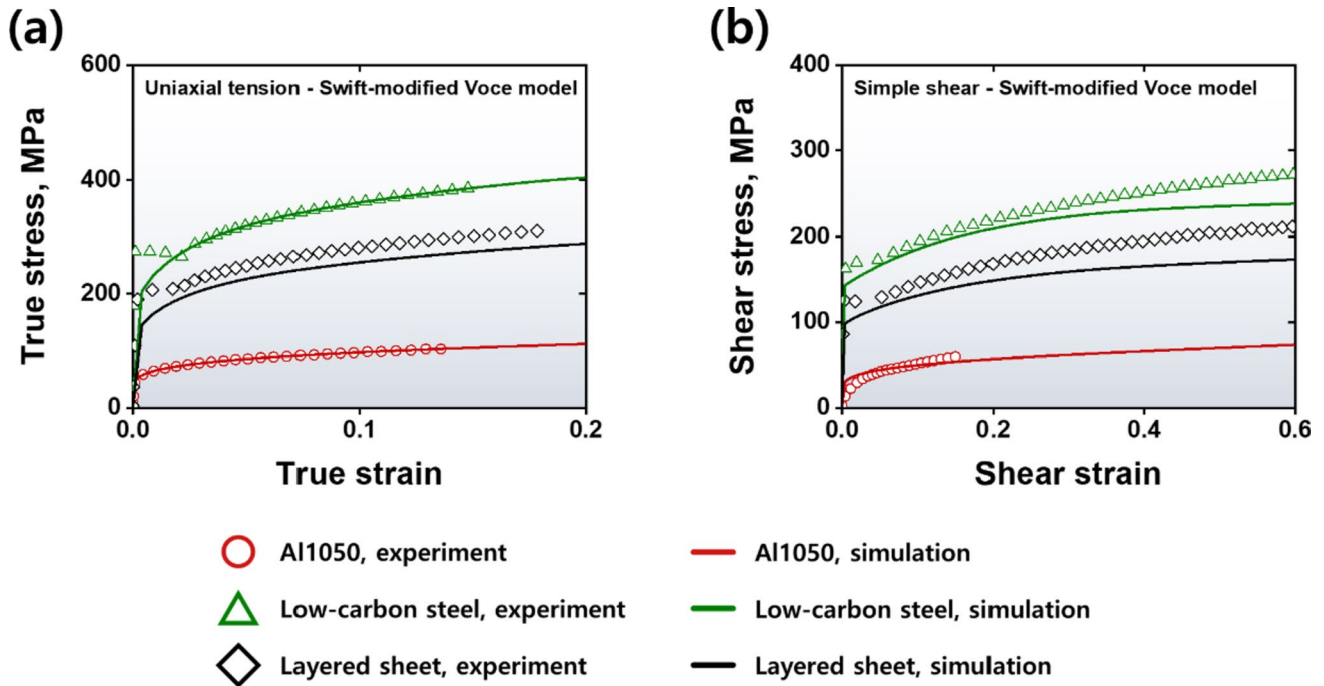


Fig. 10 **a** Numerical prediction of true stress vs. true strain curves of Al1050, low-carbon steel, and layered sheet in the tensile test using the Swift-modified Voce model; **b** Numerical prediction of shear

stress vs. shear strain curves of Al1050, low-carbon steel, and layered sheet in the simple shear test using the Swift-modified Voce model

6 Conclusions

The shear deformation behavior of heterostructured material was investigated using the Al1050/low-carbon steel/Al1050 layered sheet in this study. The BSE and EDS analyses were performed to verify the adhesive condition of the layered sheets. The EBSD analysis provided average grain sizes and GND densities. The uniaxial tensile and simple shear tests were conducted to characterize the mechanical behaviors of the Al1050, low-carbon steel, and their layered sheet. Furthermore, the microstructure and deformation mechanism-based constitutive models for the layered sheets were selected to predict mechanical behaviors. Then, the models were applied to the finite element simulations of uniaxial tensile and simple shear tests. From these experimental and numerical approaches, the following conclusions can be extracted:

- The mechanical properties of the Al1050/low-carbon steel/Al1050 layered sheet showed superior performance beyond the ROM calculation in both tensile and shear deformations. These results mainly originated from the formation of GNDs in the interface between Al1050 and low-carbon steel.
- The development of GNDs at the beginning of plastic deformation was similar in the uniaxial tension and shear deformation states. This implies that the development of

GNDs is not sensitive to deformation mode. However, the main difference between tensile and shear deformations was observed in the applied strain at maximum load. The simple shear test showed ~66% von-Mises equivalent strain at maximum shear strength but the uniaxial tensile test showed ~19% von-Mises equivalent strain at tensile UTS. The absence of plastic instability allows the development of GNDs up to large strain at maximum load, which results in more effective synergistic enhancement at maximum shear strength than tensile UTS.

- The numerical prediction of the simple shear test indicates that the dislocation density-based hardening model for the layered sheet is appropriate for simple shear deformation as well as the tensile test. This is consistent with the observation for the development of GNDs in the uniaxial tensile and simple shear tests.
- The dislocation density-based hardening model showed good extrapolation until the large strain ranges in the simple shear test. This suggests that microstructural characterization can provide reliable hardening behavior even under different deformation modes. Therefore, the dislocation density-based hardening model can be utilized for structural applications that require large strain ranges compared to the conventional phenomenological isotropic hardening model.

Acknowledgements This study was financially supported by POSCO (2023Y004) and the National Research Foundation of Korea (NRF) grant funded by the Korean government (MSIP) (NRF-2021R1A2C3006662) and (NRF-2022R1A5A1030054). Gang Hee Gu was supported by the Basic Science Research Program ‘Fostering the Next Generation of Researchers (Ph.D. Candidate)’ through the NRF funded by the Ministry of Education (RS-2023-00275651).

Data Availability Data will be made available on request.

Declarations

Conflict of interest No potential conflict of interest was reported by the author(s).

References

1. Y. Wei, Y. Li, L. Zhu, Y. Liu, X. Lei, G. Wang, Y. Wu, Z. Mi, J. Liu, H. Wang, H. Gao, Evading the strength–ductility trade-off dilemma in steel through gradient hierarchical nanotwins. *Nat. Commun.* **5**(1), 3580 (2014). <https://doi.org/10.1038/ncomm34580>
2. S. Taali, M.R. Toroghinejad, M. Kuglstatter, H.W. Höppel, Grain boundary engineering in roll-bonded copper to overcome the strength–ductility dilemma. *J. Market. Res.* **17**, 3198–3204 (2022). <https://doi.org/10.1016/j.jmrt.2022.02.032>
3. H. Yu, Y. Liu, Y. Liu, D. Wang, Y. Xu, B. Jiang, W. Cheng, L. Huang, W. Tang, W. Yu, Enhanced strength–ductility synergy in Mg–0.5 wt%Ce alloy by hot extrusion. *Met. Mater. Int.* **29**(7), 2109–2116 (2023). <https://doi.org/10.1007/s12540-022-01354-x>
4. S.-I. Lee, S.-Y. Lee, J. Han, B. Hwang, Deformation behavior and tensile properties of an austenitic Fe–24Mn–4Cr–0.5C high-manganese steel: effect of grain size. *Mater. Sci. Eng. A* **742**, 334–343 (2019). <https://doi.org/10.1016/j.msea.2018.10.107>
5. G.A. Malygin, Plasticity and strength of micro- and nanocrystalline materials. *Phys. Solid State* **49**(6), 1013–1033 (2007). <https://doi.org/10.1134/S1063783407060017>
6. G.H. Gu, R.E. Kim, J. Lee, H.S. Kim, Tailoring microstructure with spatial heterogeneity in CoCrFeMnNi high-entropy alloy via laser surface relaxation. *Mater. Sci. Eng. A* **852**, 143720 (2022). <https://doi.org/10.1016/j.msea.2022.143720>
7. D.C.C. Magalhães, O.M. Cintho, V.L. Sordi, A. Kliauga, Improved tensile properties in heterostructured 1050/7050 Al sheets produced by accumulative roll bonding. *J. Market. Res.* **17**, 2014–2025 (2022). <https://doi.org/10.1016/j.jmrt.2022.01.151>
8. X. Sun, X. Hao, J. Nie, Y. Fan, Y. Chen, S. Liu, X. Liu, Y. Zhao, Microstructure and enhanced cryogenic tensile property of a heterostructured Al–AlN/Al–Mg composite fabricated by accumulative roll bonding (ARB). *J. Market. Res.* **21**, 532–545 (2022). <https://doi.org/10.1016/j.jmrt.2022.09.037>
9. Y. Zhu, X. Wu, Heterostructured materials. *Prog. Mater. Sci.* **131**, 101019 (2023). <https://doi.org/10.1016/j.pmatsci.2022.101019>
10. Y.B. Lei, Z.B. Wang, B. Zhang, Z.P. Luo, J. Lu, K. Lu, Enhanced mechanical properties and corrosion resistance of 316L stainless steel by pre-forming a gradient nanostructured surface layer and annealing. *Acta Mater.* **208**, 116773 (2021). <https://doi.org/10.1016/j.actamat.2021.116773>
11. Q. Pan, L. Zhang, R. Feng, Q. Lu, K. An, A.C. Chuang, J.D. Poplawsky, P.K. Liaw, L. Lu, Gradient cell-structured high-entropy alloy with exceptional strength and ductility. *Science* **374**(6570), 984–989 (2021). <https://doi.org/10.1126/science.abj8114>
12. Y. Kim, G.H. Gu, H.S. Kim, Fundamental analysis of deformation behavior in core-shell heterostructured materials. *Comput. Mater. Sci.* **215**, 111818 (2022). <https://doi.org/10.1016/j.commatsci.2022.111818>
13. J. Du, G. Liu, Y. Feng, H. Feng, T. Li, F. Zhang, Strength and ductility enhancement of plain carbon steel by heterostructure design. *Mater. Sci. Eng. A* **868**, 144770 (2023). <https://doi.org/10.1016/j.msea.2023.144770>
14. W.N. Kim, S.I. Hong, Interactive deformation and enhanced ductility of tri-layered Cu/Al/Cu clad composite. *Mater. Sci. Eng. A* **651**, 976–986 (2016). <https://doi.org/10.1016/j.msea.2015.11.062>
15. G.H. Gu, R.E. Kim, E.S. Kim, Y. Kim, H. Kwon, S.Y. Ahn, M.H. Seo, H.S. Kim, Multi-scale investigation on local strain and damage evolution of Al1050/steel/Al1050 clad sheet. *J. Market. Res.* **20**, 128–138 (2022). <https://doi.org/10.1016/j.jmrt.2022.07.056>
16. Z. Yang, F. Wen, Q. Sun, L. Chai, X. Ma, M. Zhu, Strength–ductility improvement achieved by introducing heterostructured martensite in a Ti–6Al–4 V alloy. *Mater. Charact.* **192**, 112230 (2022). <https://doi.org/10.1016/j.matchar.2022.112230>
17. Z. Fu, X. Li, C. Li, H. Pan, Y. Bai, Z. Zhang, Y. Liu, Y. Liu, J. Yang, Y. Gong, C. Deng, X. Zhu, Superior mechanical properties of pure Zr with heterogeneous structure. *Mater. Charact.* **194**, 112437 (2022). <https://doi.org/10.1016/j.matchar.2022.112437>
18. J.Y. Jin, S.I. Hong, Effect of heat treatment on tensile deformation characteristics and properties of Al3003/STS439 clad composite. *Mater. Sci. Eng. A* **596**, 1–8 (2014). <https://doi.org/10.1016/j.msea.2013.12.019>
19. R.E. Kim, G.H. Gu, H. Kwon, S.Y. Ahn, J. Kwon, J.A. Lee, Y.T. Choi, M.H. Seo, H.S. Kim, Role of synergistic hardening and damage evolution on the stretchability of Al1050/steel/Al1050 sheets. *J. Market. Res.* **21**, 3514–3525 (2022). <https://doi.org/10.1016/j.jmrt.2022.10.143>
20. C. Zhao, X. Li, Quantitative study of residual strain and geometrically necessary dislocation density using HR-EBSD method. *Exp. Mech.* **61**(8), 1281–1290 (2021). <https://doi.org/10.1007/s11340-021-00741-6>
21. H. Wang, J. Ma, M. Yuan, G. Liang, X. Pei, Y. Miao, M. Li, Microstructure, deformation behaviors and GND density evolution of Ti–Al laminated composites under the incremental compression test. *Mater. Today Commun.* **33**, 104605 (2022). <https://doi.org/10.1016/j.mtcomm.2022.104605>
22. G.H. Gu, M.H. Seo, D.-W. Suh, H.S. Kim, Observation of multi-scale damage evolution in transformation-induced plasticity steel under bending condition. *Mater. Today Commun.* **34**, 105291 (2023). <https://doi.org/10.1016/j.mtcomm.2022.105291>
23. C. Brown, T. McCarthy, K. Chadha, S. Rodrigues, C. Aranas, G.C. Saha, Constitutive modeling of the hot deformation behavior of CoCrFeMnNi high-entropy alloy. *Mater. Sci. Eng. A* **826**, 141940 (2021). <https://doi.org/10.1016/j.msea.2021.141940>
24. G.R. Johnson, W.H. Cook, Fracture characteristics of three metals subjected to various strains, strain rates, temperatures and pressures. *Eng. Fract. Mech.* **21**(1), 31–48 (1985). [https://doi.org/10.1016/0013-7944\(85\)90052-9](https://doi.org/10.1016/0013-7944(85)90052-9)
25. Y.Z. Wang, Z.M. Jiao, G.B. Bian, H.J. Yang, H.W. He, Z.H. Wang, P.K. Liaw, J.W. Qiao, Dynamic tension and constitutive model in Fe40Mn20Cr20Ni20 high-entropy alloys with a heterogeneous structure. *Mater. Sci. Eng. A* **839**, 142837 (2022). <https://doi.org/10.1016/j.msea.2022.142837>
26. C. Moon, J.Y. Won, K. Lee, J. Lee, S.-W. Kim, M.-G. Lee, Mechanical behavior and interfacial damage of carbon steel–stainless steel corrosion resisted-alloy (CRA) clad plate: hybrid analysis based on experiment and finite element modeling. *Mater. Sci. Eng. A* **852**, 143697 (2022). <https://doi.org/10.1016/j.msea.2022.143697>

27. J. Zhao, M. Zaiser, X. Lu, B. Zhang, C. Huang, G. Kang, X. Zhang, Size-dependent plasticity of hetero-structured laminates: a constitutive model considering deformation heterogeneities. *Int. J. Plast.* **145**, 103063 (2021). <https://doi.org/10.1016/j.ijplas.2021.103063>
28. Y. Kim, G.H. Gu, R.E. Kim, M.H. Seo, H.S. Kim, Deformation behavior of lightweight clad sheet: experiment and modeling. *Mater. Sci. Eng. A* **852**, 143666 (2022). <https://doi.org/10.1016/j.msea.2022.143666>
29. J.S. Choi, J.W. Lee, J.-H. Kim, F. Barlat, M.G. Lee, D. Kim, Measurement and modeling of simple shear deformation under load reversal: application to advanced high strength steels. *Int. J. Mech. Sci.* **98**, 144–156 (2015). <https://doi.org/10.1016/j.ijmecsci.2015.04.014>
30. G.I. Taylor, The mechanism of plastic deformation of crystals. Part I—theoretical. *Proc. Roy. Soc. Lond. Ser a Contain. Pap. Math. Phys. Character.* **145**(855), 362–387 (1934). <https://doi.org/10.1098/rspa.1934.0106>
31. Y. Estrin, H. Mecking, A unified phenomenological description of work hardening and creep based on one-parameter models. *Acta Metall.* **32**(1), 57–70 (1984). [https://doi.org/10.1016/0001-6160\(84\)90202-5](https://doi.org/10.1016/0001-6160(84)90202-5)
32. S. Yoon, F. Barlat, Non-iterative stress integration method for anisotropic materials. *Int. J. Mech. Sci.* **242**, 108003 (2023). <https://doi.org/10.1016/j.ijmecsci.2022.108003>
33. S.-Y. Lee, H.-S. Park, J.-H. Kim, F. Barlat, K.-H. Chung, Investigation of elastic modulus degradation and recovery with time and baking process for deformed automotive steel sheets. *Met. Mater. Int.* **29**(4), 892–907 (2023). <https://doi.org/10.1007/s12540-022-01268-8>
34. S.-Y. Lee, S.-Y. Yoon, J.-H. Kim, F. Barlat, Calibration of distortional plasticity framework and application to U-draw bending simulations. *ISIJ Int.* **60**, 2927–2941 (2020). <https://doi.org/10.2355/isijinternational.ISIJINT-2020-391>
35. G.E. Dieter, D. Bacon, *Mechanical Metallurgy* (McGraw-Hill, New York, 1976)
36. J.G. Ferrero, S.S. Sweet, Evaluation of the relationship between tensile and double shear strength for various titanium alloys. in *Proceedings of the 13th World Conference on Titanium* (Wiley Online Library, 2016), pp. 965–970. <https://doi.org/10.1002/9781119296126.ch165>
37. G.H. Gu, J. Moon, H.K. Park, Y. Kim, M.H. Seo, H.S. Kim, Obtaining a wide-strain-range true stress–strain curve using the measurement-in-neck-section method. *Exp. Mech.* **61**(8), 1343–1348 (2021). <https://doi.org/10.1007/s11340-021-00747-0>
38. G.H. Gu, Y. Kim, M.H. Seo, H.S. Kim, A method for measuring plastic strain ratio over a wide strain range using the digital image correlation technology. *Met. Mater. Int.* **29**(7), 1880–1884 (2023). <https://doi.org/10.1007/s12540-022-01351-0>
39. S.-Y. Lee, S.-Y. Yoon, J.-H. Kim, F. Barlat, K.-S. Oh, Evaluation of loading-path-dependent constitutive models for springback prediction in martensitic steel forming. *Int. J. Mech. Sci.* **251**, 108317 (2023). <https://doi.org/10.1016/j.ijmecsci.2023.108317>

Publisher's Note Springer Nature remains neutral with regard to jurisdictional claims in published maps and institutional affiliations.

Springer Nature or its licensor (e.g. a society or other partner) holds exclusive rights to this article under a publishing agreement with the author(s) or other rightsholder(s); author self-archiving of the accepted manuscript version of this article is solely governed by the terms of such publishing agreement and applicable law.